Supporting Information

Lyubimov et al. 10.1073/pnas.1209406109

SI Materials and Methods

Expression and Purification of *Encephalitozoon cuniculi* Minichromosome Maintenance 2–7. Intact *Encephalitozoon cuniculi* minichromosome maintenance (*Ecu*MCM) subunits were amplified by PCR using genomic *E. cuniculi* DNA as a template and separately inserted into pFastBac transfer vectors using ligation-independent cloning (1). Each construct was engineered to include a hexahistidine (H6) -modified maltose binding protein (MBP) at the N terminus for the purposes of affinity purification. The H6MBP tag was engineered with a tobacco etch virus (TEV) protease cleavage site. The MCM-coding regions of each pFastBac vector were verified by sequencing. DH10Bac *Escherichia coli*-competent cells were transformed with the baculovirus transfer vectors carrying the *Ecu*MCM2–7 subunits and bacmids purified using the Bac-to-Bac protocol (Invitrogen). Cultured insect (Sf9) cells were transfected with individual H6MBP-fused *Ecu*MCM2–7 subunits, and freshly amplified second-generation (P2) baculovirus stock was used for large-scale expression.

The following buffers were used for the purification of the *Ecu*MCM2–7 complex: A1: 300 mM sodium acetate, 50 mM imidazole, pH 8.0, 5 mM magnesium acetate, 0.2 mM Tris(2-carboxyethyl)phosphine (TCEP), 10% (vol/vol) glycerol; A2: 300 mM sodium acetate, 50 mM imidazole, pH 8.0, 5 mM magnesium acetate, 10 mM maltose, 0.2 mM TCEP, 10% (vol/vol) glycerol; B1: 1.0 M sodium acetate, 50 mM imidazole, pH 8.0, 5 mM magnesium acetate, 0.2 mM TCEP, 10% (vol/vol) glycerol; B2: 300 mM sodium acetate, 500 mM imidazole, pH 8.0, 5 mM magnesium acetate, 0.2 mM TCEP, 10% (vol/vol) glycerol. All buffers were supplemented with a mixture of protease inhibitors: 1 μg/mL pepstatin A, 1 μg/mL leupeptin, and 1 mM phenylmethylsulfonyl fluoride (PMSF).

H6MBP-*Ecu*MCMs were expressed by coinfecting Sf9 cells in liquid culture with six viral samples of individual subunits. Using two times the *Ecu*MCM2 virus (2.0 mL/L Sf9 cells) vs. the other five subunits (1.0 mL/L Sf9 cells) resulted in the best overall yield, because *Ecu*MCM2 expressed relatively poorly and was the limiting subunit required for the formation of the complete hexamer. A total of 4.0 L Sf9 culture was inoculated and grown with shaking at room temperature for ∼72 h. The cells were then collected by gentle centrifugation (200 × *g*, Avanti JLA8.1 rotor) and resuspended in buffer B1. The cells were lysed by brief sonication (three 10-s bursts at 40 W), and the insoluble cellular debris was separated by centrifugation (30,000 × *g*, Sorwall SS-34 rotor).

The clarified lysate was passed over the nickel-charged Sepharose (GE Healthcare) column (15 mL); the column was subsequently washed with buffer B1 followed by buffer A1, at which point most of the contaminating proteins flowed through the resin. *Ecu*MCM2–7 was eluted with buffer B2 directly onto an amylose (New England Biolabs) column and washed with buffer A1. TEV protease (∼2 mg) was then loaded onto the amylose column and allowed to digest overnight at 4 °C. After 12–18 h, the H6MBP tag was cleaved from the bulk of *Ecu*MCM2–7, which was washed off the amylose column using buffer A1. The cleaved H6MBP and the uncleaved remnants of H6MBP-*Ecu*MCMs were eluted from the amylose column using buffer A2.

The cleaved *Ecu*MCM2–7 hexamer was passed over a joined pair of 1 mL prepacked cation- and anion-exchange columns (HiTrap SP and Q, respectively; GE Healthcare) preequilibrated in buffer A1. After the loading, the SP column was detached, and the Q column was washed with A1. A gradient of A1 and B1 buffers was then applied, with the *Ecu*MCM2–7 heterohexamer eluting at ∼60–70% of buffer B1 preceded by a mixture of subcomplexes and uncomplexed subunits. Finally, purified *Ecu*MCM2–7 was passed over a size-exclusion column (HiPrep 16/60 Sephacryl S-300 HR; GE Healthcare) and eluted as an intact hexamer. In some preparations, a very small secondary peak could be detected at higher retention volumes, which corresponded to detached subunits and/or subcomplexes (Fig. S3). This peak was easily separable from the main heterohexamer peak, and thus, we are confident that the final sample contained the intact heterohexameric *Ecu*MCM2–7 only. The complex was pure as determined by Coomassie-stained SDS/PAGE and monodisperse as determined by dynamic light scattering. Phosphatase treatment of *Ecu*MCM2–7 did not result in any change in the migration of individual bands by SDS/PAGE, suggesting that *Ecu*MCM2–7 is not phosphorylated by kinases present in Sf9 cells.

Biochemical Experiments. ***DNA binding assay.*** ssDNA binding activity of *Ecu*MCM2–7 was investigated by fluorescence anisotropy. The binding was carried out for 15 min at 21 °C in the following reaction buffer: 100 mM sodium acetate, 20 mM Hepes, pH 7.5, 10 mM magnesium acetate, 0.1 mg/mL BSA (Sigma), 1.0 mM TCEP, 1 mM ATP. ssDNA was kept constant at 10 nM, whereas *Ecu*MCM2–7 was titrated from 1.2 pM to 5 μM in twofold increments. Fluorescence anisotropy (FA) measurements were carried out on a Perkin-Elmer Victor 3.5 plate reader, and then, they were plotted and fitted to the Hill equation (Eq. **S1**),

$$r = \frac{\Delta FA \cdot [S]^n}{[S]^n + K_{D,app}}, \qquad \textbf{[S1]}$$

where r is the binding function, ΔFA is the change in fluorescence anisotropy proportional to the amount of ligand bound, $[S]$ is the concentration of ssDNA, $K_{D,\,app}$ is the apparent dissociation constant, and n is the Hill coefficient representing cooperativity of binding. The fitting was carried out in Kaleidagraph.

Nucleotide binding competition assay. *Ecu*MCM2–7 (1.25 μM hexamer) was preincubated with Bodipy-fluorescein–labeled ATP (Fl-ATP; 100 nM) for 15 min in 100 mM sodium acetate, 20 mM imidazole, pH 7.5, 10 mM magnesium acetate, 0.1 mM TCEP, and 0.1 mg/mL BSA. Unlabeled ATP or ATPγS was then added to the reaction at 320 nM, 40 μM, or 5 mM concentration and incubated for 20 min. FA was measured on a Perkin-Elmer Victor 3.5 plate reader. When associated with *Ecu*MCM2–7, Fl-ATP gave a higher FA signal than free Fl-ATP; displacement of Fl-ATP by unlabeled ATP or ATPγS is detected as a decrease in this signal.

ATPase assays. Initial ATP hydrolysis rates were determined using the coupled ATPase assay (2). This specific assay is advantageous, because ATP turnover can be accurately and precisely recorded in real time; additionally, ATP is regenerated by the pyruvate kinase/aldehyde dehydrogenase system, which alleviates product inhibition and substrate depletion effects on turnover rates. Measurements of WT *Ecu*MCM2–7 were performed in the ATPase reaction buffer [100 mM potassium acetate, 50 mM potassium-Hepes, pH 7.5, 10 mM magnesium acetate, 0.2 mM TCEP, 0.14 mM NADH, 0.48 mM phospho(enol) pyruvate, 10 units pyruvate kinase/aldehyde dehydrogenase mixture, 250 μg/mL BSA] in 100-μL volumes. *Ecu*MCM2–7 concentration was kept constant at 1.0 μM, whereas ATP was titrated from 0–8 mM.

Reactions were premixed in the absence of ATP in triplicate, and ATP was added immediately before measurement. Decline in NADH absorption at 530 nm was measured on a Perkin-Elmer Victor 3.5 plate reader. Initial hydrolysis rates were obtained by calculating the slope of NADH decay plotted against ATP concentration and fitted to the Michaelis–Menten equation (Eq. **S2**)

$$v = \frac{V_{max}[S]}{K_M + [S]}, \qquad \textbf{[S2]}$$

where v is the initial hydrolysis rate, V_{max} is the maximal hydrolysis rate, $[S]$ is the concentration of ATP, and K_M is the Michaelis constant, representative of the rate at 1/2$[S]$. The fitting was performed in Kaleidagraph.

Eadie–Hofstee analysis of ATPase activity. Linear plots, specifically the Eadie–Hofstee plot (v vs. $v/[S]$), can be used to detect kinetic complexity of a multisite enzyme, which could remain undetected if only the standard v vs. $[S]$ plot is used (3, 4). Specifically, when an enzyme possesses several active sites that bind the same ligand with varying affinity, the Eadie–Hofstee plot will display a distinctive deviation from linearity. This deviation is the case with all eukaryotic MCMs studied to date, *Ecu*MCM2–7 included. We were able to estimate the apparent kinetic constants of the two groups of high- and low-affinity active sites by fitting the two apparent linear regions of the Eadie–Hofstee plot to straight lines, with K_m corresponding to the slope of each line and V_{max} corresponding to the y intercept. In previous publications, the middle region of the Eadie–Hofstee plot was also fitted to a straight line, with separate kinetic constants estimated (5, 6). However, the *Ecu*MCM2–7 Eadie–Hofstee plot does not show a well-defined linear middle region. Thus, we were able to identify only two groups of active sites. This observation correlates well with the two-step ring compaction mechanism observed by small-angle X-ray scattering (SAXS).

Structural Analysis of *Ecu*MCM2–7 by EM. ***Negative-stain sample preparation.*** EM grids for apo *Ecu*MCM2-7 were prepared as follows: 400-mesh copper grids (Electron Microscopy Sciences) were coated with continuous carbon on a Nitrocellulose Amyl Acetate support using an Edwards carbon coater; holey carbon grids (C-FLATS) were used for nucleotide-bound *Ecu*MCM2-7. A 4-μL sample drop (~30 ng) was applied onto a freshly glow-discharged grid and incubated for 2 min at room temperature. The grid was sequentially laid on top of five distinct 75-μL drops of a freshly prepared 2% (wt/vol) uranyl formate solution and stirred gently for 10 s.

EM data collection. Data were collected on a Tecnai 12 transmission EM (FEI) with a Lanthanum hexaboride cathode operated at 120 keV. A magnification of 30,000× and a nominal defocus range of 1.5–0.8 μm were used. Images were acquired using the EM-MENU4 software on a TVIPS TemCam-F416 CCD camera, resulting in a final pixel size of 3.56 Å.

Particle picking and dataset generation. The EM image stack was prepared using the APPION processing environment (7). Particle picking was performed automatically using DoG picker (8). A total of 16,532 particles were extracted using the batchboxer program (9), with a box size of 64 × 64 pixels.

2D image analysis. Images were bandpass-filtered with a 180-Å high-pass cutoff and a 20-Å low-pass cutoff before alignment and classification. Reference-free class averages were produced using standard multivariate statistical analysis approaches in IMAGIC (10). On average, ~20 particles were included per class. Alignment of reference-free class averages to 2D forward projections of the final 3D volume was performed using XMIPP (11).

3D reconstruction. 3D volumes were calculated using an iterative projection-matching approach using libraries from the EMAN2 (12) and SPARX (13) packages. An initial angular increment of 30° was used, gradually decreasing to 15°. Refinement for each angular increment was iterated until >95% of the particles had a pixel error of less than 1 pixel. The resolution of the resulting 3D volume was estimated by Fourier shell correlation using the 0.5-cutoff criterion. Structure refinement using previously published EM or crystal structures of archaeal or eukaryotic MCMs as starting volumes seemed to be prone to model bias, prompting us to develop a reference-free projection-matching refinement protocol, which follows the philosophy established for 2D image analysis approaches. In brief, during traditional 2D reference-free class average calculation, a first round of classification is performed after particle-centering to a rotationally averaged total sum (a circle of diameter and gray value distribution, which matches the distribution of the particles in the dataset) (10). After a first round of alignment, iterative refinement steps are performed using the resulting class averages from a previous iteration as alignment references. During the process, the energy landscape of possible averaging solution is explored until alignment error is minimized, at which point convergence in the alignment is reached. We followed a similar approach in three dimensions: to obtain a sphere of diameter and gray-value distribution corresponding to the particles in the dataset, a volume was calculated by deliberately imposing icosahedral symmetry on one individual, randomly chosen class average. The resulting volume was subjected to Butterworth filtering, 400–350 Å range, using the fq function in Spider (14), which effectively yielded a featureless sphere, with dimensions approximating the MCM2–7 particle. As a tool for sampling different minima in the energy landscape of all possible 3D solutions, a multisphere refinement approach was used. In particular, multiple repeats of iterative two-model projection matching were performed, progressively increasing the resolution of the developing starting model, until one of two solutions revealed recognizable chirality features. This solution was, in turn, used as a starting model for multiple rounds of a single-volume projection-matching refinement until convergence was reached. The docking of atomic coordinates to the resultant 3D EM structure was carried out using University of California at San Francisco Chimera (15), whereas the rotational offsets between MCM subunits were determined in PyMOL (16).

Absolute hand determination. To determine the handedness of the Mcm2–7 ring EM map experimentally, we used tilt-pair analysis (the free-hand test) (17, 18). In brief, 0°/+50° tilt pairs were collected using a Tecnai G2 Spirit (FEI) on a 2kx2k GATAN Ultrascan 1000 camera. Particle tilt pairs were selected semi-automatically using the particle pick protocol in XMIPP (giving an average direction of tilt of 87° and an average tilt angle of +48.5°) (11) and subjected to the fast free-hand test (algorithm implemented by John L. Rubinstein, The Hospital for Sick Children, Toronto, ON, Canada) (19) using the EMAN2/SPARX projection-matching refinement routines (Python wrapper script written by Michael A. Cianfrocco, University of California, Berkeley, CA). A *Drosophila melanogaster* (*Dme*) Mcm2–7 (Mcm6-MBP) sample (51 particles) and a *Dme*CMG (Mcm3-MBP) control sample (59 particles) were deposited on C-flat grids coated with a continuous layer of carbon and stained with 2% uranyl formate (20). These particular MBP-tagged samples were chosen, because their 3D reconstructions presented the most marked chirality features compared with other related samples, also, they were distinguished by ideal particle distributions and staining quality for tilt analysis. Visual inspection of the average correlation coefficient contour map gives a strong signal, indicating that the Mcm2–7 lock washer spiral is left-handed (Fig. S6*A*, *Left*).

Difference mapping and atomic coordinate docking. To validate the results obtained from the reference-free multisphere refinement, we made use of the available EM data for two *Dme*MCM2–7 complexes substituted at the N terminus with MBP at *Dme*Mcm3 and *Dme*Mcm6, respectively. We note that those data were also

collected in the presence of nucleotide (1 mM ADP•BeF_3), and thus, they were comparable with the conditions at which the *Ecu*MCM2–7 structure was determined. We reconstructed the two fusion variants of *Dme*Mcm2–7 using the multisphere reference-free approach described above, with starting spherical models obtained from *Dme*MCM2–7 class averages (Fig. S6 *B*–*E*). We also used the final 3D volume calculated for *Ecu*Mcm2–7 as a starting model (Fig. S7*A*). In both cases, MBP-resembling electron density features were found projecting from the N-terminal subdomain A of two diametrically opposed subunits (Fig. S6*E*), consistent with the positions of *Dme*Mcm3 and *Dme*Mcm6 in the context of the left-handed open ring, which was confirmed by a direct comparison with the CMG (Fig. S7*B*). Furthermore, a density feature of *Ecu*MCM2–7 corresponding to the winged helix (WH) domain of Mcm6 (Fig. S5 *E* and *F*) could also be observed in the correct position in *Dme*Mcm2–7 density (Fig. S5*G*).

To further assess the handedness of the isolated Mcm2–7 complex, additional docking exercises were conducted on the MBP-Mcm6 fusion version of the *Dme*Mcm2–7 (Fig. S7 *C* and *D*). A striking chirality of the N-terminal collar domain is clearly visible both in the structure of the archaeal N-terminal domain and the CMG complex. Our analysis shows similar N-terminal chirality in the isolated *Dme*MCM2–7 open ring, consistent with the left-handed configuration (Fig. S7*C*). Furthermore, we carried out unsupervised docking with a tetrameric subcomplex of the archaeal six-membered N-terminal MCM collar using the *fit* function in University of California at San Francisco Chimera (15). Cross-correlation coefficients, used to quantitate the goodness of the fitting, were consistently higher for the left-handed spiral configuration compared with the right-handed spiral (Fig. S7*D*). Interestingly, three possible registers are populated by automated fitting of the MCM tetramer into the hexameric left-handed spiral (Fig. S7*D*, *Upper*), but only two registers are populated for the right-handed spiral (Fig. S7*D*, *Lower*). In the latter instance, an additional nonsensical solution appears in which the N-terminal domain is flipped, such that its C-terminal face orients away from the AAA+ tier. Taken together, these tests provide additional evidence for the left-handed, open-ring arrangement of both *E. cuniculi* and *D. melanogaster* MCM2–7 complexes.

We note that, although we submit a chirality correction for the previously published *Dme*MCM2–7 open-ring structure, the subunit order in the *Dme*Mcm2–7 assembly was determined from 2D class averages and not 3D reconstructions (20). As a consequence, the reassignment of the handedness for the *Dme*Mcm2–7 open-ring state does not alter the subunit order determined either for the Mcm2–7 or the CMG complex. Reinspection of the other models published in the work by Costa et al. (20) by these methods showed that their chirality is defined correctly and that the correction applies to the *Dme*MCM2–7 open ring only.

Structural Analysis of *Ecu*MCM2–7 by SAXS. ***Sample preparation.*** To minimize sample-to-sample variability, all SAXS experiments were performed at the same beam time shift using material from the same preparation. A single aliquot of *Ecu*MCM2–7 was used to generate 15 samples in a systematic ATPγS titration; competition assays indicate that ATPγS binds to *Ecu*MCM2–7 in a manner similar to ATP (Fig. S3*E*). Before data collection, concentrated *Ecu*MCM2–7 was dialyzed into the following buffer: 300 mM sodium acetate, 50 mM imidazole, pH 8, 5 mM magnesium acetate, 0.2 mM TCEP, 10% glycerol. The final concentration of *Ecu*MCM2–7 was 3 mg/mL, and ATPγS concentrations of 0.004, 0.008, 0.016, 0.032, 0.063, 0.125, 0.25, 0.5, 1.0, 2.0, 4.0, 6.0, 8.0, and 10.0 mM were assayed. A measurement of *Ecu*MCM2–7 in the absence of nucleotide was also obtained in the same experiment.

Data collection and processing. Scattering data were obtained at beamline 12.3.1 (SIBYLS) at the Advanced Light Source, Lawrence Berkeley National Laboratories. X-ray scattering, its applications to the determination of macromolecular shapes, and its conformations at the SIBYLS beamline are supported in part by the Department of Energy program Integrated Diffraction Analysis Technologies under Contract Number DE-AC02-05CH11231 with the US Department of Energy. Efforts to apply SAXS to characterize eukaryotic pathways relevant to human cancers are supported in part by National Cancer Institute Grant Structural Biology of DNA Repair CA92584.

Scattering from the buffer with the appropriate concentration of ATPγS but lacking *Ecu*MCM2–7 was measured before and after each protein experiment. Each sample was exposed three times for 0.5, 1, and 6 s. Because of radiation damage effects from the 6-s exposure, and high noise of the 0.5-s exposure, only 1-s exposure scattering data were used for analysis. Buffer subtraction was carried out at the beamline using SIBYLS-developed software. Buffer scattering before and after each protein measurement was subtracted separately, and the resulting curves were averaged. To eliminate scattering differences from small variations in protein concentration because of pipetting error, curves were scaled by normalization to the total scattering intensity obtained from the first (apo *Ecu*MCM2–7) experiment.

Data analysis. Plotting, preliminary analysis, and averaging of SAXS data were carried out in Primus (21). In SAXS plots, scattering intensity $I(q)$ is a function of the momentum transfer $q = (4\pi \sin\theta)/\lambda$, where 2θ is the scattering angle and λ is the wavelength of the incident beam. To emphasize scattering features, a log plot ($\log_{10}(I)$ vs. q) is commonly used to present SAXS data. For the direct analysis of nucleotide-dependent scattering change, we used Kratky plots ($I \times q^2$ vs. q), because they emphasize the changes in scattering typically obscured by the logarithmic scale. Radii of gyration (R_G) were determined from the pairwise distribution function $P(r)$ (Eq. **S3**),

$$R_G^2 = \frac{\int_0^{D_{max}} r^2 P(r) dr}{\int_0^{D_{max}} P(r) dr}, \qquad \textbf{[S3]}$$

using the full scattering curve. To minimize bias in $P(r)$ calculation, an automated procedure was used as implemented in AUTOGNOM (22). Scaling and basic tabulation of scattering data were carried out in Microsoft Excel. All plots used in figures were generated in Excel and Kaleidagraph.

Validation of ring compaction. To assess whether partial unfolding of complex might have occurred during the course of our titration, we used Kratky analyses (23, 24). In a Kratky graph, scattering intensity is multiplied by the resolution squared [$I(q)q^2$] and plotted as a function of resolution (q). This treatment results in a parabolic curve when samples are folded, whereas unfolding is detected as a rise of the scattering at higher values of q (24). Inspection of these curves for all datasets shows that *Ecu*MCM2–7 appears to be folded throughout the ATPγS titration (Fig. 5*A*). Moreover, the maximal x-axis position of the Kratky plot is dependent on the molecular weight of the particle (25). In the case of *Ecu*MCM2–7, this position does not change throughout the titration, again indicating that the heterohexamer remains intact (Fig. 4*B*). This trend also correlates with the molecular weight of the particle estimated from scattering, which remains unchanged (within a 40-kDa range or ~45–50% of the molecular weight of a single MCM subunit) throughout the ATPγS titration (Fig. S8*C*). Furthermore, the theoretical scattering curve of a modeled pentamer is distinctly different from the scattering curves observed throughout the ATPγS titration (Fig. S8*E*). Thus, it is clear that the observed particle compaction is caused by the change in ring structure

and not the loss of a subunit or any other destabilization of the *Ecu*MCM2–7 particle.

Theoretical scattering from models. Because of the scarcity of structural information for *Ecu*MCM2–7, theoretical scattering (Fig. 3*B*) had to be generated from compositionally accurate atomic models fitted into 3D EM electron density maps. As an initial basis for these models, we took the crystal structure of *Sulfolobus solfataricus* (*Sso*) MCM monomer (Protein Date Bank ID code 3F9V) (26) that was used for the interpretation of the EM density through structural fitting (Fig. 2*B*). However, the subunits of this model do not reflect natural amino acid sequence differences with *E. cuniculi* MCM subunits, and they are missing portions of the *Ecu*MCM2–7 N- and C-terminal regions. Because theoretical SAXS curves require as complete a starting model as possible, we, therefore, used the *Sso*MCM structure to create homology models of the six *E. cuniculi* MCMs using SWISS-MODEL (27). These models were then fitted into the *Ecu*MCM2–7 EM density to generate the so-called EM model (Fig. 3*B*, red) and fitted into the previously published *Dme*MCM2–7 open-ring EM density (20) to generate the so-called *Dme*MCM2–7 model (Fig. 3*B*, green). To generate the closed-ring model (Fig. 3*B*, purple), we aligned *Ecu*MCM2–7 homology models to the hexameric model of *Sso*MCM (26). Finally, we generated a skewed EM model (Fig. 3*B*, blue) by applying a 5° intersubunit rotation around the ring along the axis drawn between the C-terminal helices of the adjacent subunits; this axis placement yielded a theoretical scattering change most similar to the change observed by experiment. Automated model fitting into EM density was carried out in University of California at San Francisco Chimera (15, 28), whereas theoretical curves were generated using the online FoxS server (29).

Curve-Fitting. ***Fitting to the Michaelis–Menten equation.*** Small-angle scattering and the global parameters that can be extracted from it (e.g., R_G) represent the average contribution to scattering of all of the particles in the sample, and thus, they can be used to study structural equilibria of multistate systems in solution (23, 30). Given that the observed nucleotide-dependent changes in scattering seemed to correspond to specific structural transitions in *Ecu*MCM2–7 (specifically, ring compaction; discussed above and in the text), we attempted to quantitate these structural transitions by plotting changes in scattering (from specific points on the Kratky plot) as well as the global R_G vs. ATPγS concentration. In all cases, saturation/decay plots were obtained, suggesting that all of the scattering changes in question correspond to the accumulation of the compacted ring species observed at high nucleotide concentrations. As a result, these plots could be readily fitted to a general binding equation (Eq. **S4**),

$$r = \frac{\Delta sig[S]}{K_{app} + [S]}, \qquad \textbf{[S4]}$$

where r is the general saturation function, represented by either R_G or $I \times q^2$ extracted from the Kratky plot, Δsig is the change in signal (also either R_G or $I \times q^2$) that we interpret as proportional to the number of bound sites, $[S]$ is the concentration of ATPγS ,and K_{app} is an apparent pseudoequilibrium constant for the observed structural transition. We expressed K_{app} as K_{Rg} for R_G and K_{k1} and K_{k2} for the constants derived from Kratky analysis. The fitting was reasonable in all cases ($R = 0.92$ for R_G and $R = 0.94$ and $R = 0.99$ for $I \times q^2$ at $q = 0.03$Å^{-1} and $q = 0.07$Å^{-1}, respectively). All plotting and curve-fitting was done in Kaleidagraph.

Fitting to the two-site binding model. The two different pseudoequilibrium constants obtained by analysis of SAXS results agree with the Eadie–Hofstee analysis of the *Ecu*MCM2–7 ATPase activity, and they highlight the existence of two groups of active sites in the complex, with differing affinities for the substrate. Given these observations, we attempted to fit the SAXS plots to a two-site binding equation (Eq. **S5**),

$$r = \frac{\Delta sig_1[S]}{K_{app,1} + [S]} + \frac{\Delta sig_2[S]}{K_{app,2} + [S]}, \qquad \textbf{[S5]}$$

where the constants are the same as in Eq. **S4**, with the exception of two independent pseudoequilibrium constants ($K_{app,1}$ and $K_{app,2}$), and the assumption of two populations of independent binding sites (Δsig_1 and Δsig_2). All three SAXS plots could be fitted to the two-site model reasonably well, resulting in R values equal to the values obtained from the corresponding single-site models (Fig. S8 *F*–*H*). The pseudoequilibrium constants extracted from these fits are in remarkable agreement with each other, with $K_{Rg,1} = 0.015 \pm 0.16$ mM and $K_{Rg,2} = 0.17 \pm 0.30$ mM from the R_G plot (Fig. S8*F*), $K_{k1,1} = 0.014 \pm 0.87$ mM and $K_{k1,2} = 0.21 \pm 0.37$ mM from the low q ($q = 0.03$ Å^{-1}) plot (Fig. S8*G*), and $K_{k2,1} = 0.018 \pm 0.018$ mM and $K_{k2,2} = 0.17 \pm 0.45$ mM from the medium q ($q = 0.07$ Å^{-1}) plot (Fig. S8*H*).

It is clear from the above results that both the large-scale, global architectural rearrangements as well as the smaller-scale, localized conformational changes contribute to the changes in scattering at both low and medium q ranges. However, inspection of Δsig values shows that these contributions differ. Specifically, at low q, $\Delta sig_1 = 0.003$, whereas $\Delta sig_2 = 0.009$, suggesting that the second transition is favored ($K_{k1,2} = 0.21 \pm 0.37$ mM). Indeed, this constant is highly similar to the constant obtained from the single-site model fit of the same data ($K_{k1} = 0.24 \pm 0.11$ mM). Likewise, at medium q, $\Delta sig_1 = -0.014$, whereas $\Delta sig_2 = -0.005$ (negative values reflect the fact that this curve is a decay rather than saturation curve), favoring the first transition ($K_{k2,1} = 0.018 \pm 0.018$ mM), which is also consistent with the pseudoequilibrium constant obtained from the single-site fit of the same plot ($K_{k2} = 0.032 \pm 0.01$ mM). In sum, both one- and two-site binding models yield essentially the same pseudoequilibrium constants.

These results recapitulate the conclusions from the single-site binding model: namely, that *Ecu*MCM2–7 ring compaction is a two-step process, with $K_{app,1} \sim 0.02$ mM and $K_{app,2} \sim 0.2$ mM ATPγS. However, the large errors indicate that, despite the high degree of correspondence between the estimated pseudoequilibrium constants, these data are not of sufficient quality to be fit to the more complex models with confidence. Consequently, we chose to report the pseudoequilibrium constants extracted from fitting our data to the single-site binding model rather than to two-site solutions.

1. Aslanidis C, de Jong PJ (1990) Ligation-independent cloning of PCR products (LIC-PCR). *Nucleic Acids Res* 18(20):6069–6074.
2. Lindsley JE (2001) Use of a real-time, coupled assay to measure the ATPase activity of DNA topoisomerase II. *Methods Mol Biol* 95:57–64.
3. Bisswanger H *Enzyme Kinetics: Principles and Methods*, trans Bubehneim L (2002) (Wiley, New York), pp 26-28.
4. Hofstee BH (1952) On the evaluation of the constants Vm and KM in enzyme reactions. *Science* 116:329–331.
5. Ilves I, Petojevic T, Pesavento JJ, Botchan MR (2010) Activation of the MCM2-7 helicase by association with Cdc45 and GINS proteins. *Mol Cell* 37:247–258.
6. Schwacha A, Bell SP (2001) Interactions between two catalytically distinct MCM subgroups are essential for coordinated ATP hydrolysis and DNA replication. *Mol Cell* 8:1093–1104.
7. Lander GC, et al. (2009) Appion: An integrated, database-driven pipeline to facilitate EM image processing. *J Struct Biol* 166:95–102.
8. Voss NR, Yoshioka CK, Radermacher M, Potter CS, Carragher B (2009) DoG Picker and TiltPicker: Software tools to facilitate particle selection in single particle electron microscopy. *J Struct Biol* 166:205–213.
9. Ludtke SJ, Baldwin PR, Chiu W (1999) EMAN: Semiautomated software for high-resolution single-particle reconstructions. *J Struct Biol* 128:82–97.

10. van Heel M, Harauz G, Orlova EV, Schmidt R, Schatz M (1996) A new generation of the IMAGIC image processing system. *J Struct Biol* 116:17–24.
11. Scheres SH, Núñez-Ramírez R, Sorzano CO, Carazo JM, Marabini R (2008) Image processing for electron microscopy single-particle analysis using XMIPP. *Nat Protoc* 3:977–990.
12. Tang G, et al. (2007) EMAN2: An extensible image processing suite for electron microscopy. *J Struct Biol* 157:38–46.
13. Hohn M, et al. (2007) SPARX, a new environment for Cryo-EM image processing. *J Struct Biol* 157:47–55.
14. Frank J, et al. (1996) SPIDER and WEB: Processing and visualization of images in 3D electron microscopy and related fields. *J Struct Biol* 116:190–199.
15. Pettersen EF, et al. (2004) UCSF Chimera—a visualization system for exploratory research and analysis. *J Comput Chem* 25:1605–1612.
16. DeLano WL (2002) *The PyMOL User's Manual* (DeLano Scientific, San Carlos, CA).
17. Henderson R, et al. (2012) Outcome of the first electron microscopy validation task force meeting. *Structure* 20:205–214.
18. Rosenthal PB, Henderson R (2003) Optimal determination of particle orientation, absolute hand, and contrast loss in single-particle electron cryomicroscopy. *J Mol Biol* 333:721–745.
19. Lau WC, Baker LA, Rubinstein JL (2008) Cryo-EM structure of the yeast ATP synthase. *J Mol Biol* 382:1256–1264.
20. Costa A, et al. (2011) The structural basis for MCM2-7 helicase activation by GINS and Cdc45. *Nat Struct Mol Biol* 18:471–477.
21. Konarev PV, Volkov VV, Sokolova AV, Koch MHJ, Svergun DI (2003) PRIMUS: A Windows PC-based system for small-angle scattering data analysis. *J Appl Crystallogr* 36:1277–1282.
22. Petoukhov MV, Konarev PV, Kikhney AG, Svergun DI (2007) ATSAS 2.1 - towards automated and web-supported small-angle scattering data analysis. *J Appl Crystallogr* 40:S223–S228.
23. Bernadó P, Svergun DI (2012) Structural analysis of intrinsically disordered proteins by small-angle X-ray scattering. *Mol Biosyst* 8:151–167.
24. Putnam CD, Hammel M, Hura GL, Tainer JA (2007) X-ray solution scattering (SAXS) combined with crystallography and computation: Defining accurate macromolecular structures, conformations and assemblies in solution. *Q Rev Biophys* 40:191–285.
25. Semisotnov GV, Timchenko AA, Melnik BS, Kimura K, Kihara H (2003) Kratky plot as a tool to evaluate the molecular mass of globular proteins. *Proton Factory Activity Rep B* 20:256.
26. Brewster AS, et al. (2008) Crystal structure of a near-full-length archaeal MCM: Functional insights for an AAA+ hexameric helicase. *Proc Natl Acad Sci USA* 105: 20191–20196.
27. Bordoli L, Schwede T (2012) Automated protein structure modeling with SWISS-MODEL Workspace and the Protein Model Portal. *Methods Mol Biol* 857: 107–136.
28. Meng EC, Pettersen EF, Couch GS, Huang CC, Ferrin TE (2006) Tools for integrated sequence-structure analysis with UCSF Chimera. *BMC Bioinformatics* 7:339.
29. Schneidman-Duhovny D, Hammel M, Sali A (2010) FoXS: A web server for rapid computation and fitting of SAXS profiles. *Nucleic Acids Res* 38:W540–W544.
30. Blobel J, Bernadó P, Svergun DI, Tauler R, Pons M (2009) Low-resolution structures of transient protein-protein complexes using small-angle X-ray scattering. *J Am Chem Soc* 131:4378–4386.

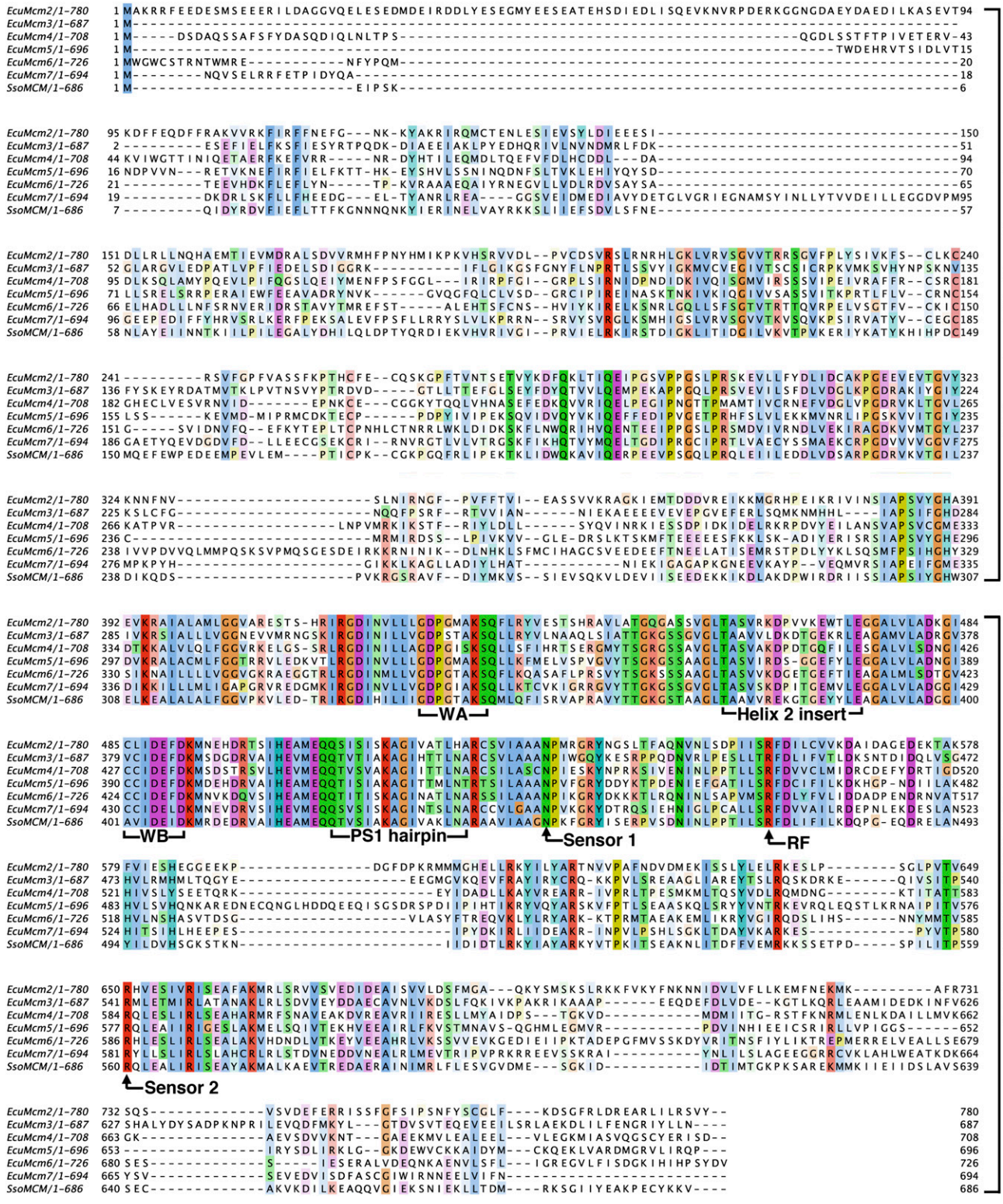

Fig. S1. *Ecu*MCMs are minimized eukaryotic MCM proteins. Multiple sequence alignment of complete *Ecu*MCM2–7 sequences with *Sso*MCM are shown with conserved domains and AAA+ elements indicated. RF, arginine finger motif; WA, Walker A motif; WB, Walker B motif. Conservation is highlighted by ClustalX coloring (1) as rendered in JalView (2).

1. Chenna R, et al. (2003) Multiple sequence alignment with the Clustal series of programs. *Nucleic Acids Res* 31:3497–3500.
2. Waterhouse AM, Procter JB, Martin DM, Clamp M, Barton GJ (2009) Jalview Version 2—a multiple sequence alignment editor and analysis workbench. *Bioinformatics* 25:1189–1191.

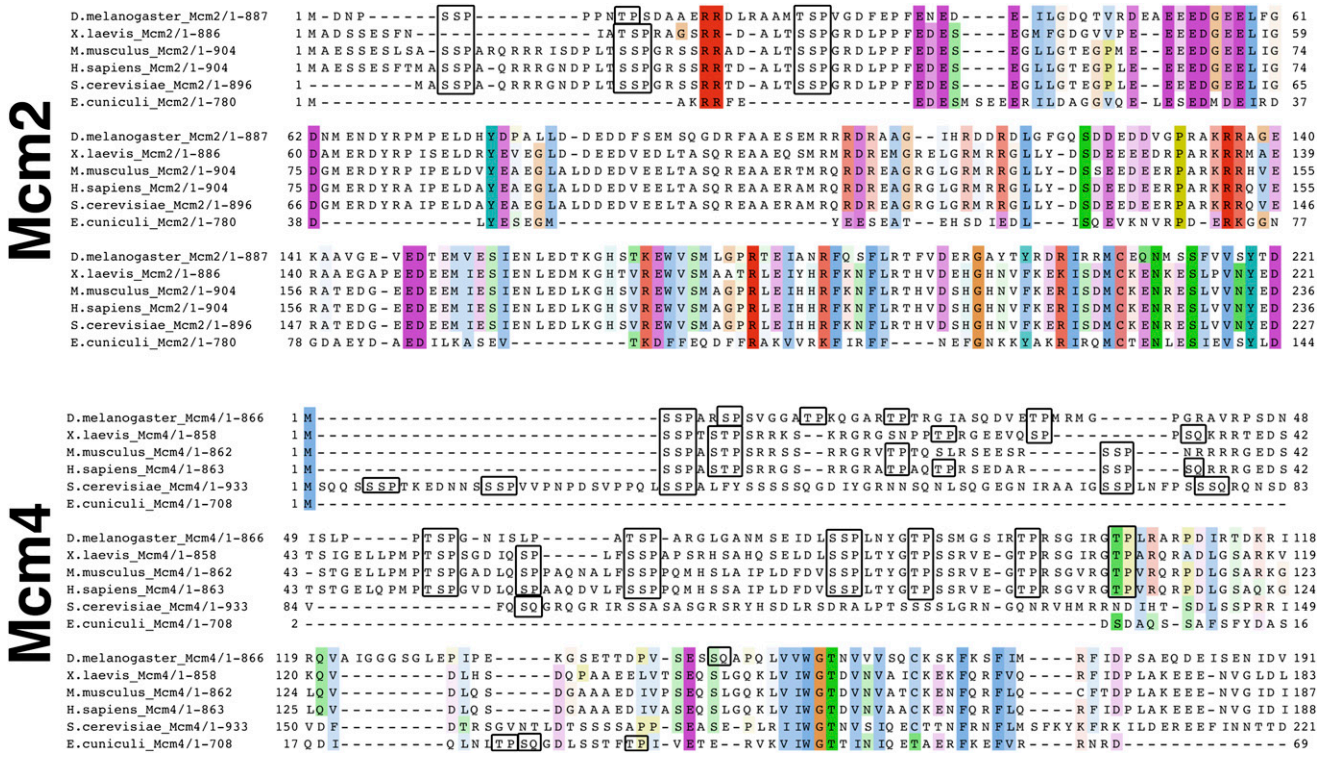

Fig. S2. *Ecu*MCMs lack nearly all regulatory phosphorylation sites found in other eukaryotic MCMs. Multiple sequence alignments of N-terminal regions of *Ecu*MCM2 (*Upper*) and *Ecu*MCM4 (*Lower*) with respect to corresponding selected metazoan and fungal genera. Conservation is highlighted by ClustalX coloring (1) as rendered in JalView (2). Potential N-terminal phosphorylation sites [some of which have been verified for cell-cycle kinases CDK and Dbf4-dependent Cdc7 kinase (DDK) as well as ATR/Mec1 in yeast] are boxed. Note the near complete absence of such sites and indeed, the N-terminal regions themselves in *Ecu*MCM2 and *Ecu*MCM4.

1. Chenna R, et al. (2003) Multiple sequence alignment with the Clustal series of programs. *Nucleic Acids Res* 31:3497–3500.
2. Waterhouse AM, Procter JB, Martin DM, Clamp M, Barton GJ (2009) Jalview Version 2—a multiple sequence alignment editor and analysis workbench. *Bioinformatics* 25:1189–1191.

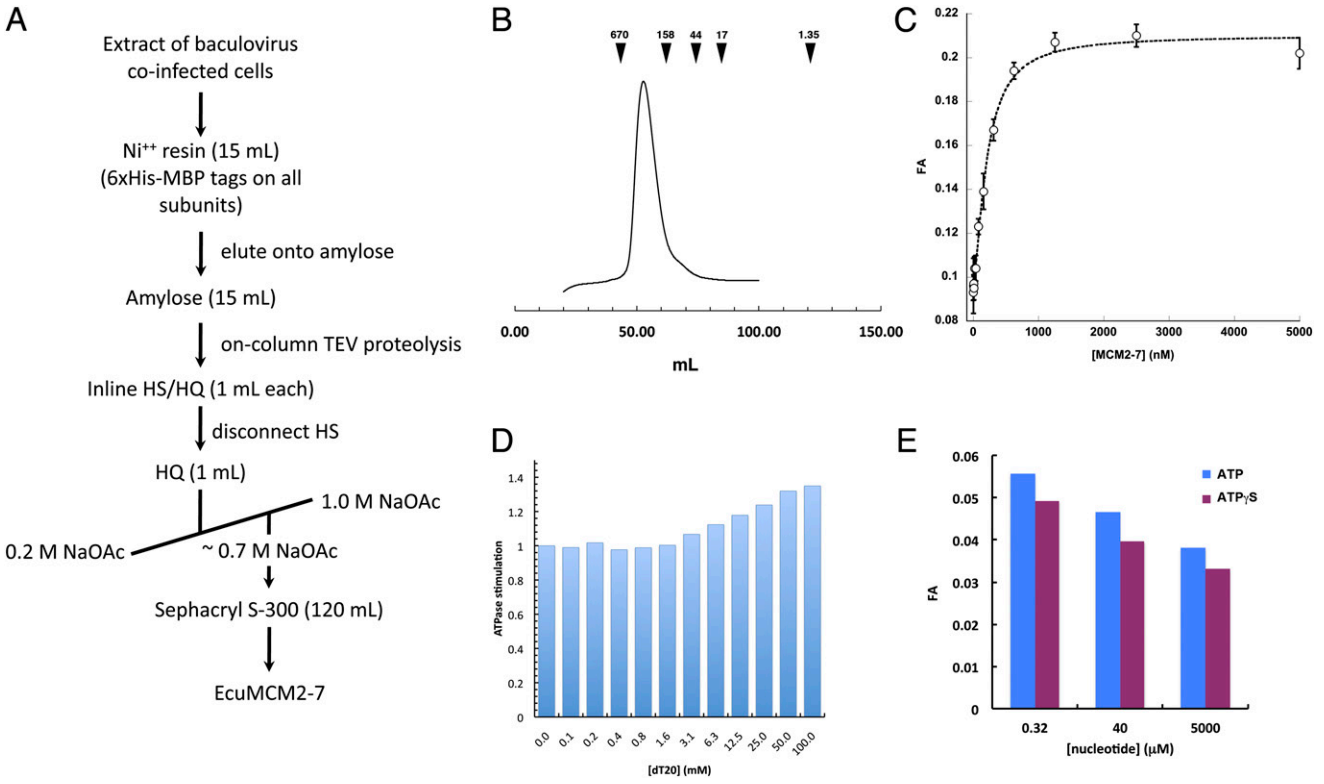

Fig. S3. Expression, purification, and characterization of *Ecu*MCM2–7. (*A*) Purification scheme used to obtain intact *Ecu*MCM2–7 complex. (*B*) Size-exclusion chromatography (SEC) of intact *Ecu*MCM2–7; molecular weight standards (kDa) are indicated with arrows. (*C*) ssDNA (36-mer) binding by *Ecu*MCM2–7 in the presence of 1.0 mM ATP obtained by fluorescence anisotropy (apparent K_D ~ 200 nM). (*D*) Stimulation of ATPase activity by ssDNA (dT_{20}). The maximal stimulation of ~1.3-fold was achieved at 1,000-fold molar excess of ssDNA. (*E*) ATP (blue) and ATPγS (red) compete similarly for the binding of fluorescently labeled ATP to *Ecu*MCM2–7. Binding of unlabeled nucleotide is demarcated as a decrease in fluorescence anisotropy (FA) signal.

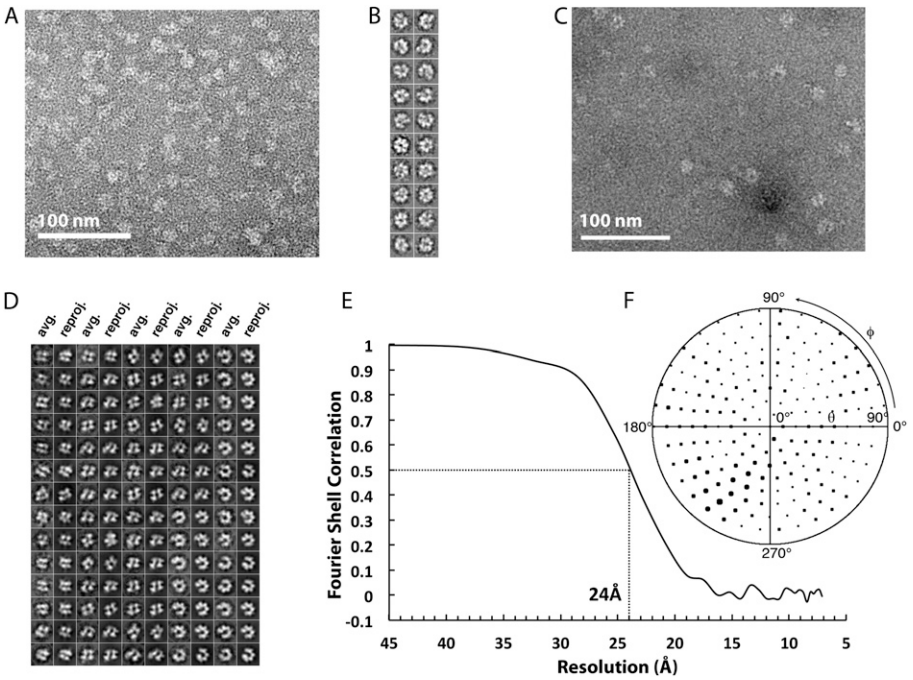

Fig. S4. EM data for apo and ATPγS-bound *Ecu*MCM2–7. (*A*) Sample electron micrograph of apo *Ecu*MCM2–7. (*B*) Reference-free class averages of apo *Ecu*MCM2–7. (*C*) Sample electron micrograph of *Ecu*MCM2–7 + 10mM ATPγS. (*D*) Reference-free class averages compared against matching forward projections of the 3D lock washer structure. (*E*) Fourier shell correlation (FSC) plot for the final cycle of projection-matching refinement (*SI Materials and Methods*), with resolution estimated by the 0.5 criterion. (*F*) Euler angle distribution for class averages obtained for *Ecu*MCM2–7 + 10 mM ATPγS. The size of each dot is representative of the number of images corresponding to the given Euler angle.

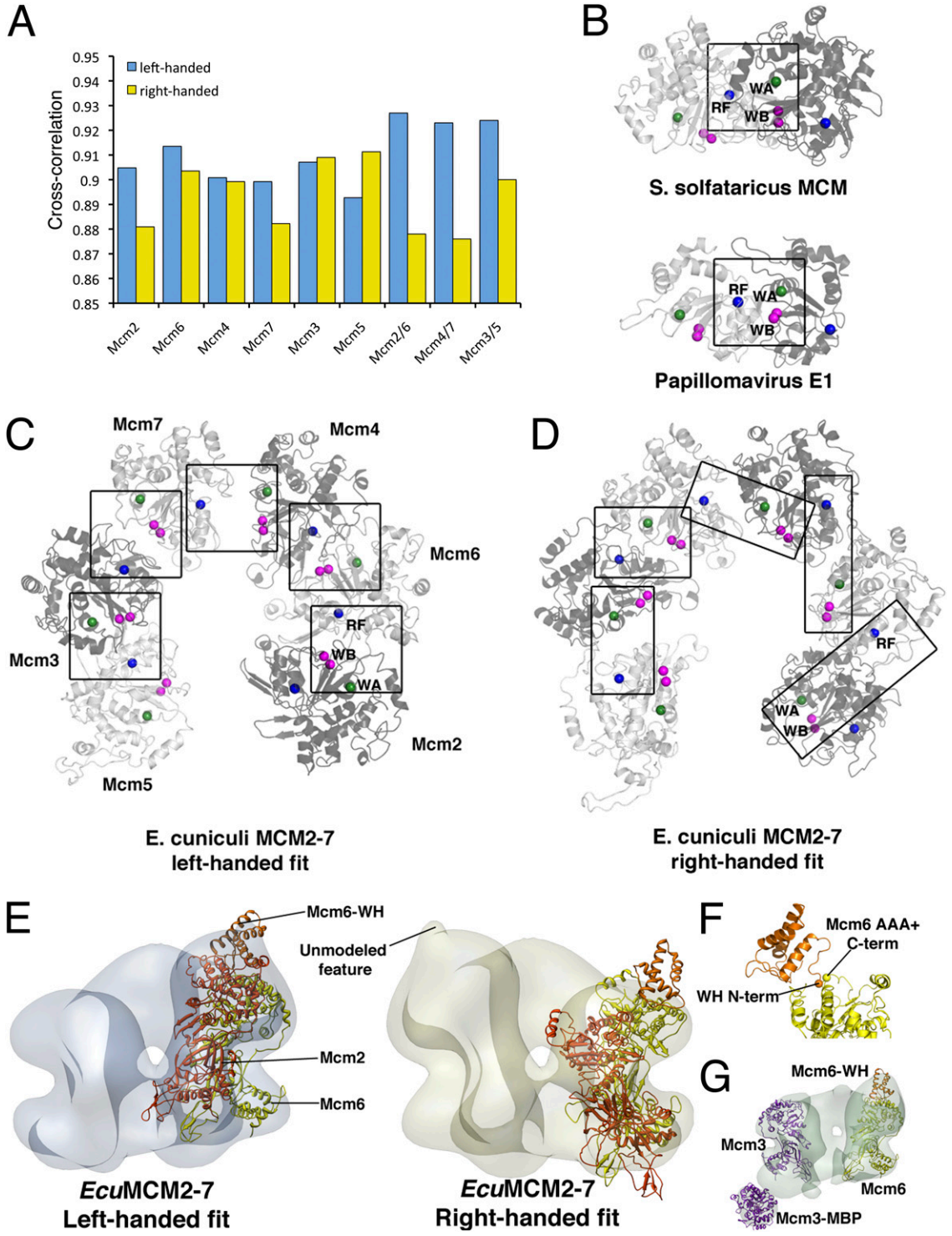

Fig. S5. A left-handed lock washer reconstruction yields proper ATPase site alignment and Mcm6 WH domain localization after computationally defined model fitting. (*A*) Cross-correlation (CC) coefficients of *Sso*MCM monomers (Protein Data Bank ID code 3F9V) and modeled dimers as fitted into the EM density of left-handed (blue bars) and right-handed (yellow bars) *Ecu*MCM2–7 rings. (*B*) ATPase site alignment of modeled *Sso*MCM (*Upper*) (1) and papillomavirus E1 (*Lower*; Protein Data Bank ID code 2GXA) (2) dimers. (*C* and *D*) ATPase site alignment resulting from crystal structure fitting into left-handed (*C*) and right-handed (*D*) *Ecu*MCM2–7 EM density. Only AAA+ domains are shown for clarity; the ATPase sites in all interfaces are boxed. Blue sphere, RF; green sphere, WA; magenta sphere, WB. (*E*) Fitting of the Mcm6-WH (Protein Data Bank ID code 2KLQ) (3) into a prominent feature seen in electron density maps for a left-handed (*Left*) and right-handed (*Right*) *Ecu*MCM2–7 EM model. Note that the domain fits into a feature protruding from the ATPase domains of left-handed maps. By contrast, this feature is unaccounted for in the right-handed maps, whereas the MCM6-WH domain is left exposed. Only Mcm2 (red), Mcm6 (yellow), and the Mcm6-WH domain (orange) are shown for clarity. (*F*) Cartoon representation of the C-terminal portion of Mcm6 AAA+ domain (yellow ribbon) and the Mcm6-WH domain (orange ribbon), with the C terminus of the AAA+ domain (yellow ball) and the N terminus of the WH domain (orange ball) highlighted to show that automated fitting of WH domain into left-handed EM density preserves the continuity of the Mcm6 structure. (*G*) Fitting of the Mcm6-WH domain into the left-handed *Dme*MCM2–7(Mcm6::MBP) density. Only Mcm6 (yellow), Mcm6-WH (orange), Mcm3 (purple), and Mcm3-MBP (purple) are shown for clarity.

1. Brewster AS, et al. (2008) Crystal structure of a near-full-length archaeal MCM: Functional insights for an AAA+ hexameric helicase. *Proc Natl Acad Sci USA* 105:20191–20196.
2. Enemark EJ, Joshua-Tor L (2006) Mechanism of DNA translocation in a replicative hexameric helicase. *Nature* 442:270–275.
3. Wei Z, et al. (2010) Characterization and structure determination of the Cdt1 binding domain of human minichromosome maintenance (Mcm) 6. *J Biol Chem* 285:12469–12473.

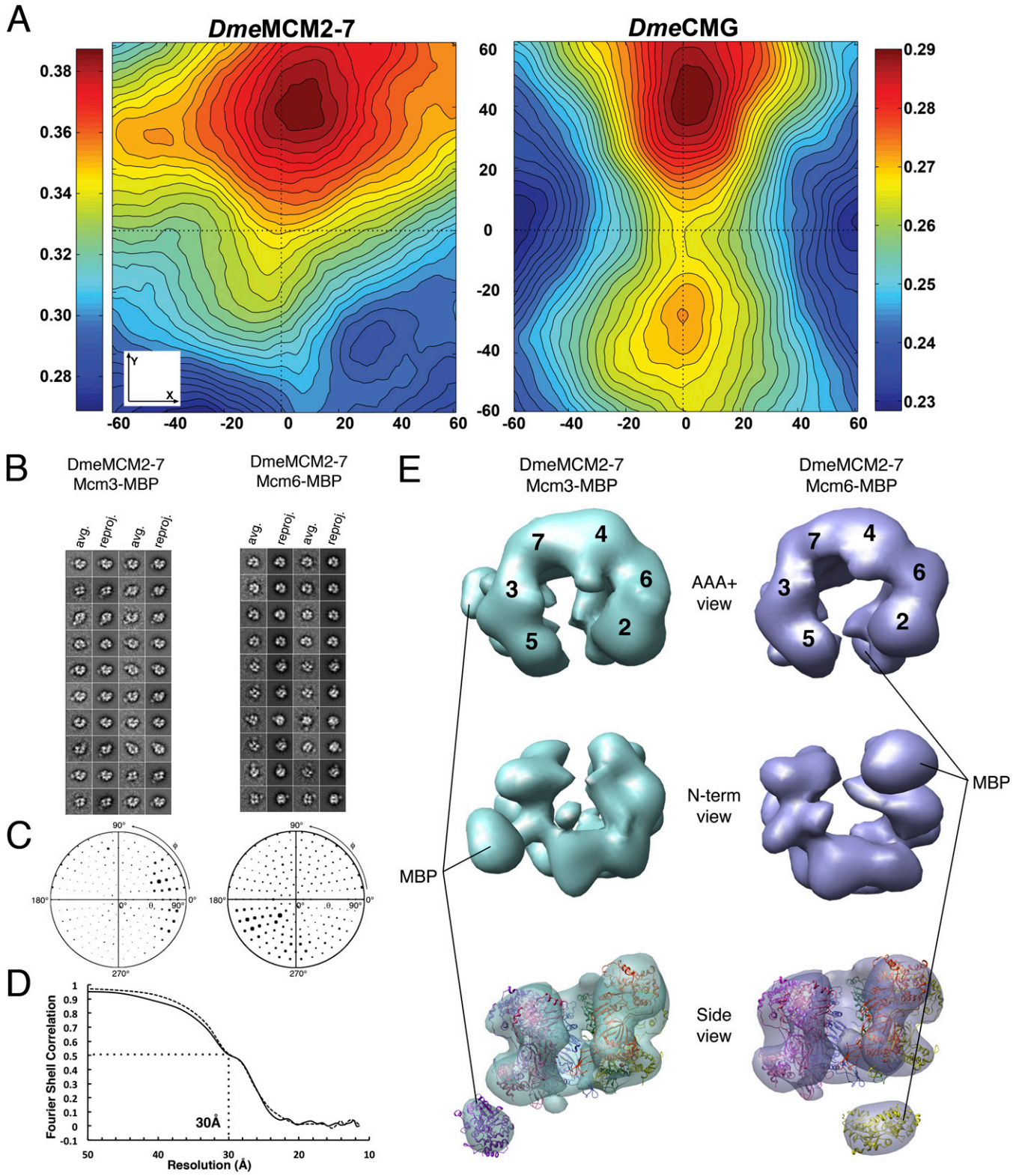

Fig. S6. Free-hand test and structure determination of MBP-modified *Dme*MCM2–7. (*A*) Average correlation coefficient for *Dme*Mcm2–7-Mcm6MBP (*Left*) and *Dme*CMG-Mcm3MBP (*Right*) particles collected at a nominal 50° tilt angle and 90° tilt direction angle. The strong correlation peak mapping corresponds to

Legend continued on following page

~50° (tilt) and ~90° (tilt direction). These maps are consistent with a left-handed and not right-handed *Dme*MCM2–7 open ring. (*B*) Reference-free class averages compared with forward reprojections of the 3D reconstructions obtained for (*Left*) *Dme*MCM2–7(Mcm3-MBP) and (*Right*) *Dme*MCM2–7(Mcm6-MBP). (*C*) Respective Euler angle distributions for particles used in 3D reconstitution. The size of each dot represents the number of particles corresponding to the Euler angle. (*D*) FSC plot for Mcm3-MBP (solid line) and Mcm6-MBP (dashed line), with approximate resolution indicated using the 0.5 criterion. (*E*) 3D reconstruction of (*Left*) *Dme*MCM2–7(Mcm3-MBP) and (*Right*) *Dme*MCM2–7 (Mcm6-MBP). Perspectives are as follows: *Top Left*, AAA+ face; *Middle Left*, N-terminal face; *Bottom Left*, Mcm5/2 gate. *Sso*MCM and MBP structures fitted into EM density are shown in ribbon representation and colored according to the same scheme as in Fig. 2.

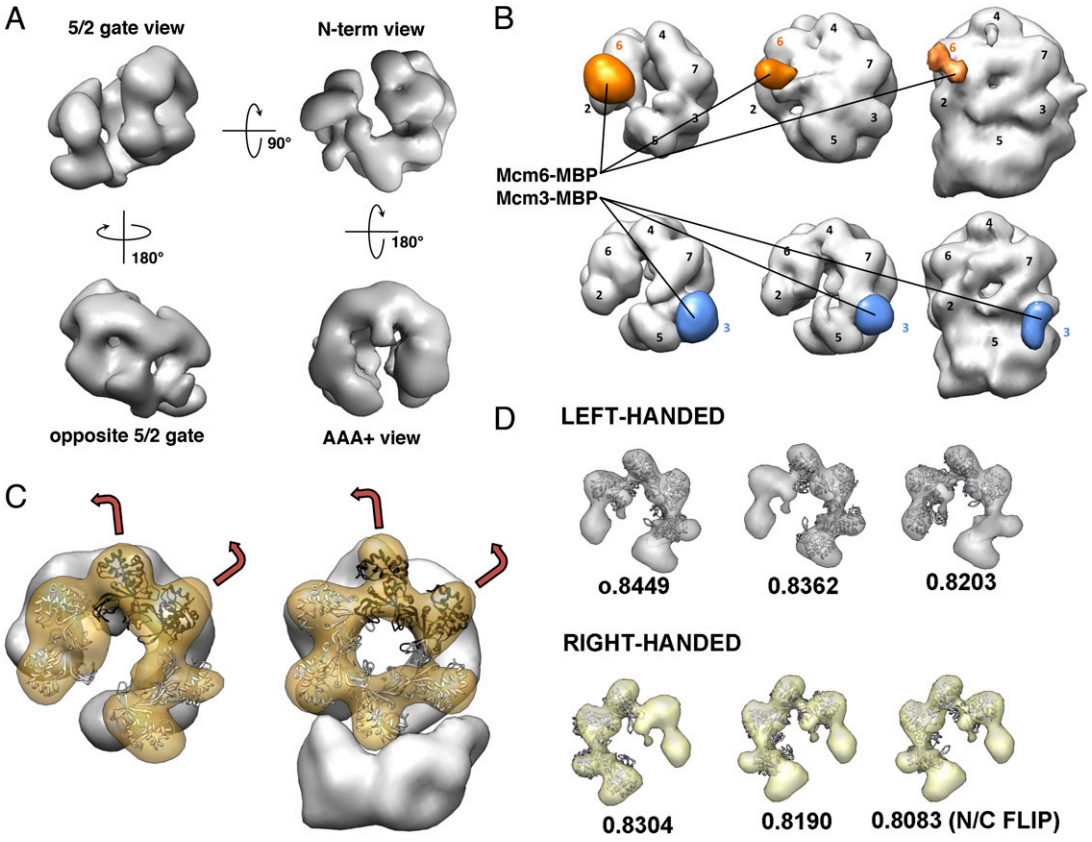

Fig. S7. Additional validation of chirality of left-handed *Dme*MCM2–7 EM reconstruction. (*A*) Structure of the *Dme*MCM2–7(Mcm6::MBP) calculated using *E. cuniculi* MCM2–7 EM density (Fig. 2) as a starting model. The map is displayed at a contour that does not allow visualization of the MBP tag but that highlights chirality features. (*B*) Structure of the MBP-tagged versions of Mcm6 (*Upper*) or Mcm3 (*Lower*) within the isolated MCM2–7 (*Left* and *Center*) or the Cdc45•MCM2–7•GINS assembly (CMG; *Right*). The MCM2–7 structure was calculated either using a sphere (*Left*) or the *E. cuniculi* structure (*Center*) as a starting model. (*C*) Docking of the *Methanothermobacter thermautotrophicus* MCM N-terminal domain into the *Dme*MCM2–7 open ring or the CMG electron density map. A counterclockwise propeller feature in the N-terminal domain, recognizable in the atomic coordinates as well as the EM maps, is highlighted with red arrows. (*D*) Cross-correlation coefficients calculated for the first three best docking solutions of a tetrameric archaeal N-terminal domain subcomplex into the two mirror versions of an isolated N-terminal domain lock washer.

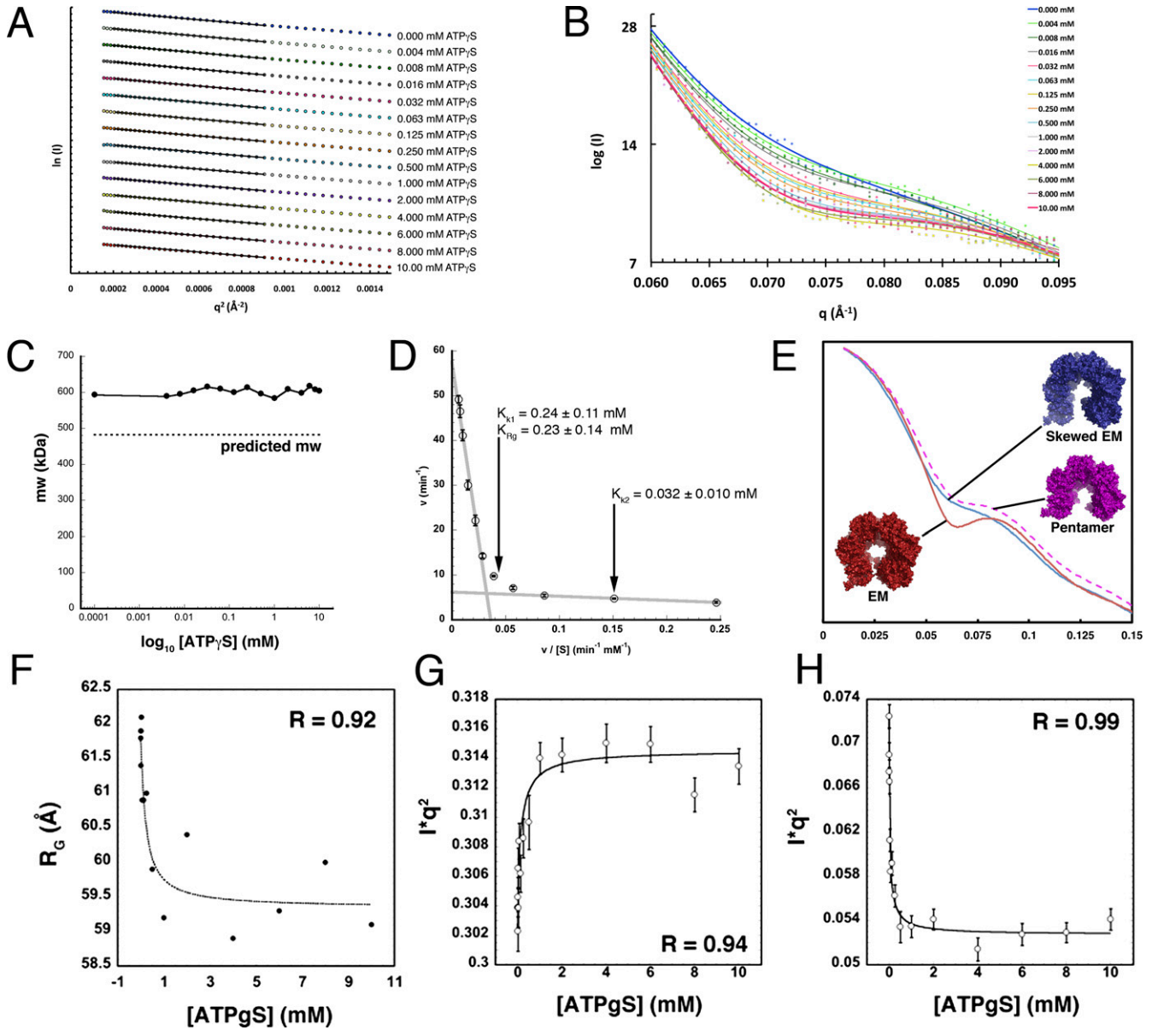

Fig. S8. Analysis of *Ecu*MCM2–7 dynamics by SAXS . (*A*) Guinier regions of the scattering curves of *Ecu*MCM2–7 in the presence of varying levels of nucleotide (indicated on the right). The linear portion of the Guinier region is indicated with solid straight lines. The absolute intensity of each scattering plot was adjusted by an arbitrary coefficient to facilitate side-by-side comparison. (*B*) Scattering change at medium angles (~60–100 Å). Raw data are shown in dots, and smoothed curves (from GNOM) (22) are shown as solid lines. The color scheme is the same as in Fig. 4*A*. (*C*) Estimated molecular weight (from Porod volume) (*SI Materials and Methods*) of *Ecu*MCM2–7 samples plotted vs. nucleotide concentration. (*D*) Pseudoequilibrium constants of structural transitions detected by SAXS mapped onto an Eadie–Hofstee plot of *Ecu*MCM2–7 ATPase activity (Fig. 1*D*); K_{Rg} is the pseudoequilibrium constant obtained from the plot of R_G vs. [ATPgS], whereas K_{k1} and K_{k2} are pseudoequilibrium constants obtained from plotting the change in scattering ($I \times q^2$; from the Kratky plot) at $q = 0.03$ Å^{-1} (K_{k1}) and $q = 0.07$ Å^{-1} (K_{k2}). (*E*) Theoretical scattering curves for the EM-based *Ecu*MCM2–7 model (red), the skewed EM-based model (blue), and a prospective model for an *Ecu*MCM2-6 pentamer (magenta and dotted line). The systematic offset of the pentamer scattering curve from the hexameric models (and the observed data) indicates that the complex has not dissociated. (*F–H*) Two-site binding model fits of (*F*) R_G vs. [ATPγS], (*G*) low q ($q = 0.03$ Å^{-1}) Kratky scattering vs. [ATPγS], and (*H*) medium q ($q = 0.07$ Å^{-1}) Kratky scattering vs. [ATPγS].

Table S1. Numbers of predicted phosphorylation sites in *D. melanogaster* and *E. cuniculi* MCM2–7 complexes

	CDK	DDK	ATR
D. melanogaster			
Mcm2	4 (3)	2 (1)	2 (2)
Mcm3	4 (2)	1	4 (2)
Mcm4	17 (12)	4 (4)	6 (1)
Mcm5	0	0	2
Mcm6	2 (1)	0	3 (1)
Mcm7	2	0	2
Total	29 (18)	7 (5)	19 (8)
E. cuniculi			
Mcm2	0	0	2
Mcm3	2	0	2
Mcm4	5 (2)	0	7 (1)
Mcm5	4	0	3
Mcm6	3	1	2
Mcm7	3	0	1
Total	17 (2)	1*	17 (1)

The frequency of occurrence for S/T-P (CDK), S/T-Q (ATR), and S-S/T-P/Q (DDK) sequences found in both systems is shown. Numbers in parentheses correspond to the number of predicted sites that are conserved in other eukaryotes.

*The single DDK sequence found in *E. cuniculi* is not conserved, and it was found in the AAA+ domain of *Ecu*Mcm6 rather than the N-terminal domain, where most of the verified DDK phosphorylation sites were located in yeast MCMs. Thus, it is likely to be spurious and not an actual DDK site.

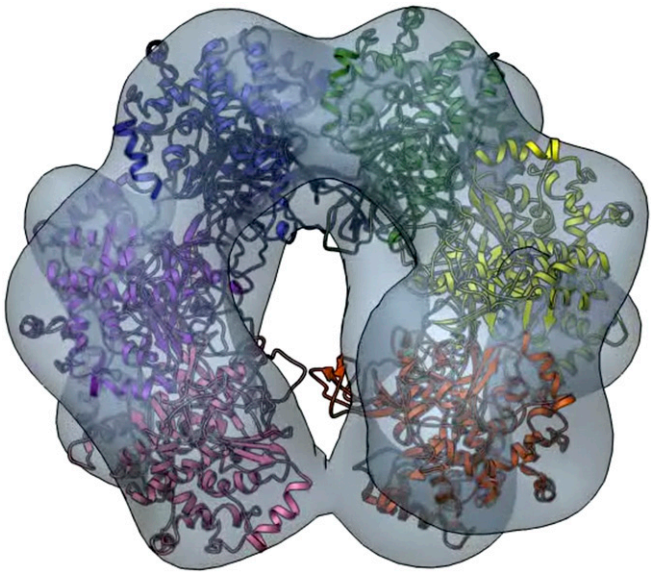

Movie S1. Single-particle 3D EM reconstruction of *Ecu*MCM2–7. The 3D reconstruction is shown first as a solid volume, then as a semitransparent volume with fitted crystal structures of six *Sso*MCM monomers (shown in cartoon representation), and finally, as a segmented volume. The coloring of individual MCM monomers and EM density segments follows the same scheme as in Fig. 2.

Movie S1